Quaternary Science Reviews 85 (2014) 85–98

Contents lists available at ScienceDirect

Quaternary Science Reviews

journal homepage: www.elsevier.com/locate/quascirev

Chronology and paleoenvironmental records of a drill core in the central Tengger Desert of China

Zaijun Li, Donghuai Sun*, Fahu Chen, Fei Wang, Yuebao Zhang, Feng Guo, Xin Wang, Baofeng Li

Key Laboratory of Western China's Environment Systems (Ministry of Education), Research School of Arid Environment & Climate Change, Lanzhou University, Lanzhou 730000, China

ARTICLE INFO

Article history:
Received 2 April 2013
Received in revised form
16 November 2013
Accepted 2 December 2013
Available online 25 December 2013

Keywords:
Asian drying
Tibetan Plateau uplift
Chronology
Tengger Desert

ABSTRACT

The desertification history of inland Asia provides most direct evidence for Asian drying history, but the formation ages of the most Asian deserts are not clear due to the lack of outcrops. The Tengger Desert, one of the main proximal deserts of the Chinese Loess Plateau (CLP), is of special paleoclimatic significances for its dust emission and environmental affection. Here, we report lithofacies, paleomagnetic ages and paleoenvironmental proxy indexes of the first drill core (WEDP01) from the central Tengger Desert. Paleomagnetism measurements reveal that the core spans from ~3.55 Ma to present, consistent with the electron spin resonance (ESR) dating results. The strata of the central desert consist of alluvial–fluvial deposits, lacustrine–fluvial deposits mixed with dust, and eolian sand from bottom to top. Sedimentary analysis reveals that continuous eolian sand started by ~0.9 Ma, marking the initial formation of the Tengger Desert; and the domination of eolian sand in the strata with similar characters of the modern desert appeared by ~0.68 Ma, indicating expansion of the Tengger Desert. The proximal deserts formation and simultaneous increase of dust accumulation in the CLP and the North Pacific Ocean in mid-Pleistocene demonstrate the role of proximal deserts for the dust loading of Northern China and even Northern Hemisphere. Our analysis suggests the uplift of Tibetan Plateau in the mid-Pleistocene probably played the main role for this drying event and desert formation, while global cooling may strength the arid environment of the proximal deserts.

1. Introduction

The aridification in the Asian interior is one of the most predominant paleoenvironmental events during the Cenozoic. The loess-red clay sequences in the Chinese Loess Plateau (CLP), products of the Asian aridification, have been used broadly to reveal the drying history of the Asian interior. Studies on these eolian sequences indicate that eolian deposits start to accumulate on the main CLP since ~7–8 Ma (Ding et al., 1998; Sun et al., 1998a,b; Qiang et al., 2001; Song et al., 2007), indicating possible initiation timing of Asian aridification. These studies also found stepwise aridification intensified at 3.6–3.4, 2.8–2.4 and 1.2–0.6 Ma (e.g. Kukla and An, 1989; Chen et al., 1991, 2001; Guo et al., 2004; An et al., 2005; Ding et al., 2005; Wang et al., 2007; Wu et al., 2007; Sun et al., 2008), as signaled by changes in paleoenvironmental proxy records, such as grain-size, sedimentary accumulation rates, intensity of chemical weathering and paleoecology. Subsequent works proposed that eolian deposits started to accumulate on the western CLP as early as 22 Ma (Guo et al., 2002), or 25 Ma (Qiang et al., 2011), signaling an earlier onset of Asian aridification and desertification. Although much knowledge has been acquired based on loess-red clay sequences from the CLP, little is known about the dust source areas. The most direct evidence for aridification and desertification of the Asian interior comes from Asian deserts themselves (Zhu et al., 1980; Wu, 2009; Sun et al., 2011a).

The deserts in northwestern China were conventionally divided into distal and proximal deserts according to distance from the CLP (Liu, 1985; Ding et al., 2000; Wu, 2009). The main distal deserts include the Taklimakan Desert, the Gurbantunggut Desert, the Qaidam Basin Desert and the Kumtag Desert; while main proximal deserts include the Badain Jaran Desert, the Tengger Desert, the Mu Us Desert, the Ulan Buh Desert and the Hobq Desert (Fig. 1a). A previous research at Mazartag in the central Taklimakan Desert suggested that it was formed at 7.2 Ma (Sun et al., 2009), but a recent study based on new paleomagnetic dating of two parallel sections indicated that formation of the Taklimakan Desert should

* Corresponding author. Fax: +86 931 8912330.
E-mail address: dhsun@lzu.edu.cn (D. Sun).

0277-3791/$ – see front matter © 2013 Elsevier Ltd. All rights reserved.
http://dx.doi.org/10.1016/j.quascirev.2013.12.003

be about 3.4 Ma (Sun et al., 2011a). A work on the loess record in Yutian, southern edge of Tarim Basin, dated the bottom age of the loess section as ~0.88 Ma, and showed an abrupt increase of grain-size and calcium carbonate proportion around ~0.5 Ma (Fang et al., 2002a). A more recent 207 m loess drill core in the Pulu area, close to Yutian, revealed that grain-size stepwise increased at ~0.87 and ~0.5 Ma (Zan et al., 2010). These two loess studies may indicate step-by-step expansion of the Taklimakan Desert around ~0.9–0.8 and ~0.5 Ma.

Relative to the distal Taklimakan Desert, the proximal deserts are more important in terms of contributing dust to the CLP (e.g., Ding et al., 2000; Sun, 2002; Zhang et al., 2003; Sun et al., 2004; Lü and Sun, 2011), but few studies have been applied to the proximal deserts due to the lack of outcrops in these deserts. Tengger Desert, the largest proximal desert directly upwind to the CLP, is regarded as one of the most important sources for the CLP (Liu, 1985; Liu et al., 1994; Zhang et al., 1997, 2003; Sun, 2002; Rao et al., 2006; Chen et al., 2007; Lü and Sun, 2011). However, only few loess sequences on the edge of the desert have been examined to investigate desertification history of this area. The bottom age of the Wuwei loess section suggested that the Tengger Desert has existed before ~0.85 Ma (Guan et al., 2011). In this study, we report chronology studies of a drill core (WEDP01) in the central Tengger Desert and explore its implications for the desertification in Asian interior and the significance of paleoclimate.

2. Geological setting and drilling

The Tengger Desert, located in the southeast of the Alxa Plateau, is surrounded by the Yabulai Mountains to the north, the Eastern Qilian Mountains to the southwest, and the Helan Mountains to the east (Fig. 1b). The modern mean annual precipitation and temperature in this area are 100–200 mm and 7.0–9.7 °C, respectively (Wu, 2009). The modern Tengger Desert is dominated by W–NNW winds but influenced by SE–E winds during the summer half year (Zhang et al., 2008).

The Tengger Desert is covered by dunes in most places, and a few outcrops of Tertiary and Mesozoic strata appear scatterly in the desert (Wu, 2009). Stratigraphic surveys in the Tengger desert region reveal that the Tertiary deposits contain the Chaganbulage formation and the Ganhegou formation. Paleontological evidence suggests that the Chaganbulage formation is late Eocene strata (Wang and Wang, 1997), which consists of fuchsia mudstone and sandy mudstone in the northeastern and eastern edge of the Tengger Desert near the Helan Mountains. The Ganhegou formation, probably deposited in Pliocene based on evidence from the fossils of *Hipparion* sp. and *Elasmotheriidae indet* in the southern Tengger Desert, were divided into three parts (Cao et al., 1985): the lower part consists of brownish red sandy mudstone, muddy sandstone and sandy gravels; the middle part consists of brownish red sandy mudstone with gray yellow carbonate concretions; and the upper part consists of brownish red muddy sandstone and sandy gravels.

More than 400 small lakes are developed in the desert, most of which are the remnants of Tertiary lakes. Precipitation and spring water are major water sources of these lakes (Wu, 2009). The WEDP01 core was drilled near the shore of a salt lake (Chahanchi Lake), located in the center of the Tengger Desert (38° 22′42″ N, 104° 39′17″ E) (Fig. 1b).

276 m strata are drilled totally for WEDP01 core, and 171.48 m drill core (diameter 75 mm) was recovered with a mean core recovery rate of 62% (78% between 0 and 147 m, 50% between 147 and 276 m) from July to September, 2008. The recovered sediments consist mostly of clay, silt, and fine sand, whereas medium to coarse sand and gravels cannot be collected completely during drilling because they are unconsolidated and easy to fall out from the barrel. The beddings of strata are nearly horizontal and the section contains five sedimentary units from the bottom to the top:

Unit 1: brownish red sandy–gravels mudstone interbedded with gravels layers (201.94–276 m), typical gravels layers appear at 209.06–217.98 m and 251.78–256.01 m. The micro-bedding was invisible in the most sandy–gravels mudstone. These lithologic characters are consistent with the lower part of the Ganhegou formation.
Unit 2: brownish red sand interbedded with muddy sand and sandy gravels (147–201.94 m), the sandy gravels layers are located at 176.45–182.38 m and 147–150.83 m. Between 182.38 and 201.94 m and 157.48–176.45 m, the brownish red sand and muddy sand layers contain carbonate concretions. This unit may be corresponded to the middle and upper Ganhegou formation.
Unit 3: thin layers of red sandy clay interbedded with thin layers of sand (147–78.9 m) with the exception of 124.15–129.41 m where gray gravels dominate.
Unit 4: reddish silty clay interbedded with silt (78.9–48.3 m) with obvious micro-bedding.
Unit 5: yellow to light yellow sand interbedded with white and gray–green carbonate-sand (48.3–0 m). Carbonate concretions are visible between 28.99 and 48.3 m.

3. Sampling and measurements

3.1. Sampling

The recovered drill core was firstly cut into 2 cm thick slices perpendicularly to the core axis, and further cut into 2 cm cubes as paleomagnetic samples. The remaining was collected for powder sample. Five ESR dating samples were collected from the upper 30 m core with an interval of ~5 m and saved in sealed iron tubes.

3.2. Rock magnetism measurement and paleomagnetic measurements

1196 paleomagnetic samples were selected with an interval of ~10–20 cm, or 2–5 cm in few sand and gravels layers for thermal demagnetization using a MMTD80 thermal demagnetizer. The remanent magnetization was measured with a 2G Enterprise 760 Cryogenic Magnetometer. Both the demagnetizer and the magnetometer are installed in a shielded room with a residual field of less than 200 nT. 36 pilot specimens with 5–10 m interval were demagnetized with steps of 30 °C from room temperature to 690 °C, and the rest of the samples were demagnetized with steps of 30, 40 and 50 °C from room temperature to 600 °C or 690 °C. The demagnetization results were evaluated using orthogonal projection (Zijderveld, 1967) diagrams. ChRM directions were calculated using a principal component analysis (PCA) of least-squares method (Kirschvink, 1980). All the paleomagnetic data was analyzed using PMGSC (V4.2) developed by R. Enkin.

37 samples with 5–10 m interval were selected for magnetic hysteresis and thermomagnetic analysis to determine the magnetic carriers of the remanent magnetization. The hysteresis loops measurements were performed with a variable field translation balance (VFTB) using a maximum field of 1 T. The temperature dependence of magnetization was measured using VFTB from room temperature (~20 °C) to 700 °C and then back to room temperature with an interval of 4 °C in 110 mT applied field. Magnetic hysteresis loops are presented after removing contribution from paramagnetic materials, which was calculated from the slope between 800 and 1000 mT of original loops.

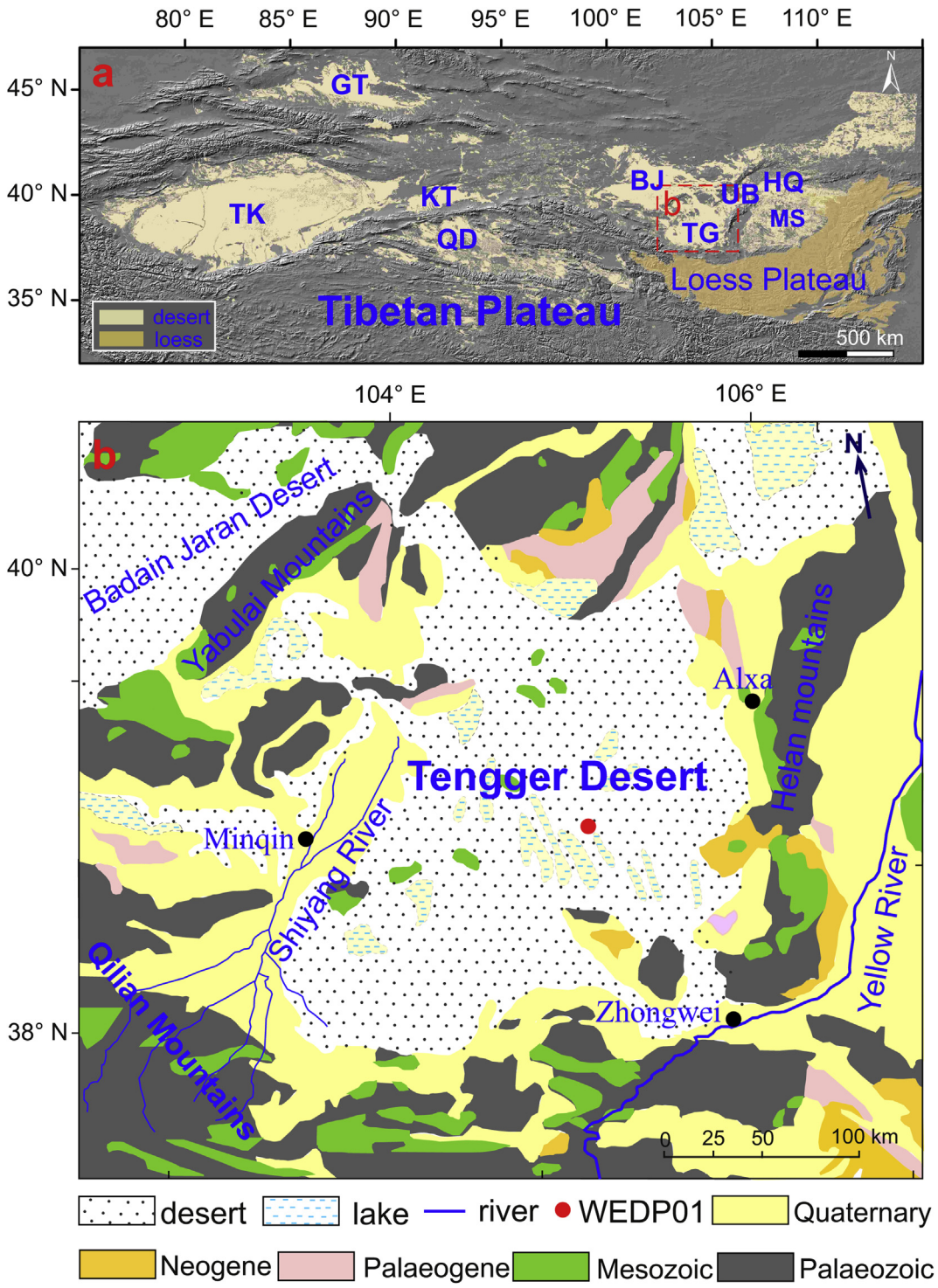

Fig. 1. Desert distribution of Northwestern China (a) and the location map of the WEDP01 core in the Tengger Desert (b). TK – Taklimakan Desert, GT – Gurbantunggut Desert, KT – Kumtag Desert, QD – Qaidam Basin Desert, BJ – Badain Jaran Desert, TG – Tengger Desert, UB – Ulan Buh Desert, HQ – Hobq Desert, MS – Mu Us Desert. Deserts distribution data is provided by the Environmental and Ecological Science Data Center of West China, National Natural Science Foundation of China (http://westdc.westgis.ac.cn). Figure (b) is modified from the 1:2,500,000 geologic map of China.

3.3. ESR dating

The five ESR dating samples were treated following the pre-treatment procedure method of Yin et al. (2007). One aliquot of quartz grains and six aliquots of bleached quartz grains (125–180 μm) were analyzed on the X-band ESR spectrometer (Bruker EMX 2.7/8). The ESR spectra of quartz Ti–Li centers were measured at 77 K with microwave power 5 mW, sweeping width 350 G, modulation amplitude 1.6 G, modulation frequency 100 kHz, time constant 40.96 ms, and sweep time 41.94 s. The uranium and thorium contents were obtained in a Daybreak 530 Model alpha counter. The potassium contents were determined by an HG5 flame

photometer. Water concentrations were also weighed and taken into account.

3.4. Sedimentary facies analysis methods

Methods employed for sedimentary faces analysis include core sediment property observation, grain-size and grain morphology analysis. In general, alluvial–fluvial deposits are easily distinguished by their chaotic characteristics consisting of clay, sand and gravels. In contrast, lacustrine deposits are of horizontal bedding and laminas. However, it is difficult to distinguish eolian deposits from lacustrine sediments if eolian sand and dust depositing in water and owning sedimentary features of lacustrine deposits in arid areas, such as in the Qinghai Lake, the largest lake in China (An et al., 2012), and the Sudan Lake, a salt lake in Qaidam Basin (Qiang et al., 2007). Grain-size component and grain morphology analysis provide ways to solve this problem.

3.4.1. Grain morphology analysis

Ten pilot samples from modern dunes and typical layers of the core were selected for Scanning Electro Microscope (SEM) analysis. Samples (~ 1 g) were first treated with 10% H_2O_2 to remove organic matter, and then with 10% HCl at 100 °C to remove carbonate. Dispersed grains were washed with distilled water to remove the superfluous H_2O_2 and HCl, and then dried at room temperature. The grain morphology was observed on a Hitachi S4800 SEM.

3.4.2. Grain-size measurement and sedimentary origin analysis

For grain-size analysis, 281 drill core samples were selected with an interval of approximate 1 m; and four modern dune samples in the central Tengger Desert also be collected for contractive analysis. Samples were first separated into two components with a sieve: >2 mm portion and <2 mm portion. For the >2 mm portion, samples were then further sieved with sieves of different sizes. For the <2 mm portion, samples were treated with 10% H_2O_2 to remove organic matter, and then treated with 10% HCl to remove carbonate. After standing for about 24 h, samples were dispersed with 10% $(NaPO_3)_6$ and ultrasonicated. Then, samples were measured with a Malvern Mastersizer 2000 laser grain-size analyzer.

Based on the grain-size distribution data, Grin-size component analysis method (Sun et al., 2002, 2004, 2008, 2011a,b; Wang et al., 2013) is used to analyze the size, proportion and origins of all components consisting in each sample. In the method, grain-size components are firstly determined and the grain-size distribution functions are set. Then, sizes and proportions of all constituting components are calculated through grain-size distribution function fitting. Finally, the origins of all components are analyzed according to the frequency distribution of sizes and proportions of whole components of all samples of the record with references of other sedimentary information.

3.4.2.1. Component determination. On frequency curve of grain-size distribution, almost all samples of the strata are poly-modal sediments. Commonly, most components can be clearly identified on frequency curve if their components are not overlapped strongly (Sun et al., 2002, 2004, 2008, 2011a,b). On frequency curve of strong overlapping of components, they can also be carefully identified by distinguishing the non-smooth knee point. After component determination, the function type of each component was determined. Weibull and Normal are found to be suitable functions for most sediments (Sun et al., 2002, 2011b). Component determination and function type selection can be checked and modified with fitting results indicated by residual error in the following step.

3.4.2.2. Function fitting. After determining components and function types of all components, the grain-size function formula for a sample was defined as the sum of each component (Sun et al., 2002). In order to obtain best fitting result with minimum fitting error between calculated function values and measured grain-size data, three choices were provided: 1) re-selecting function type of the components that do not acquire best fitting, 2) adding one or more components on function formula, 3) repeating fitting procedure. After fitting, the modal sizes and proportions of all components were calculated. In calculating, modal size of each component is used to represent the size parameter. Modal size of a sample or component is defined as the size of such fraction that has the highest proportion in all fractions of the sample or component.

3.4.2.3. Origin analysis. According to the lithological characteristics and the fitting results, the origin of each sedimentary component of the obviously typical sediments in WEDP01 core has been firstly recognized. The typical eolian sand type (Fig. 2b 1–2) exhibits tri-modal grain-size distribution which is composed of an overwhelmingly dominant eolian saltation (eolian sand) component (modal size ~220 μm), a minor short-term suspension dust (coarse eolian dust) component and a long-term suspension dust (fine eolian dust) component. The modal size of the eolian sand components of the four dune samples is 223.5, 220.9, 237.4 and 243.1 μm, respectively. The fluvial deposit type (Fig. 2b 5) shows a poly-modal grain-size distribution with an overwhelming dominant fluvial saltation (fluvial sand) component (modal size ~400 μm), which is coarser than eolian saltation component. The alluvial deposit type (Fig. 2b 6) displays a poly-modal distribution as well, but the proportion of fluvial saltation component is less than in fluvial deposits. The lacustrine sand in small inland lake with small eroded zone is fundamentally transported from rivers (Hakanson and Jansson, 1983), and thus the lacustrine sand component could be recognized as the fluvial sand component in modal size. The eolian dust deposits in the WEDP01 core are not as pure as the loess, and commonly mixed with other original deposits; but its characteristic short-term suspension component, as same as the coarse component in loess, could be recognized easily on the grain-size frequency curve (Fig. 2b 4). Eolian dust components are also popularly found in WEDP01 core as minor components, such as in eolian sand-domination deposits (Fig. 2b 3) and hydrogenic domination deposits (Fig. 2b 5, 6).

Due to the sizes and proportions of sediments with different origins have their specific ranges (e.g. Ashley, 1978; Bagnold and Barndorff-Nielsen, 1980), components with specific origins are grouped on modal size and proportion frequency distribution of all components of whole samples of the strata when plotted on same frequency plots, which can also be used as tools to determine origin for some components whose origins are not easily identified (Sun et al., 2011b; Wang et al., 2013). Fig. 3 shows these three types of statistic plots of WEDP01 core. The frequency distribution of modal sizes (Fig. 3a) not only provide a way to show the modal size range of a specific original component, but also serve as a tool to distinguish component origin when comparing to the typical origin components modal size. Similarly, the frequency of the proportion (Fig. 3c) is used to determine the proportion range of the components, especially for the components which have the same modal size, such as the eolian, fluvial and lacustrine long-term suspension components. Meanwhile, the "modal size-proportion" plot (Fig. 3b) is a result showing the distribution of different origin components.

Five different groups are identified according to the combination of inflections at 2, 11, 120, 298 μm on the modal size–frequency curve (Fig. 3a). The group between 0 and 2 μm is the ultrafine pedogenic component (Sun et al., 2011c), nearly separated in every samples and with the modal size between 0.7 and 0.8 μm; the

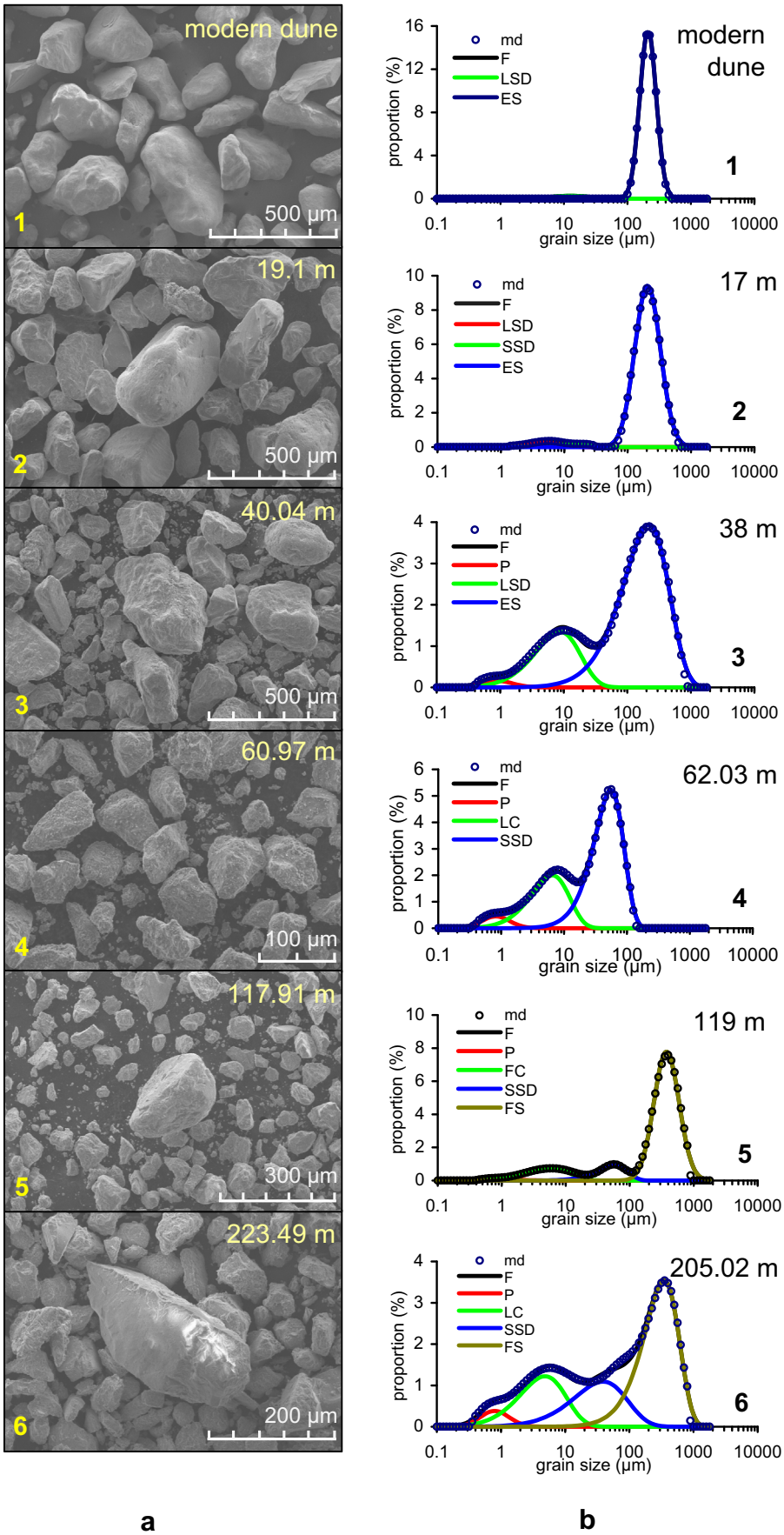

Fig. 2. SEM images (left) and grain-size distribution (right) of typical samples for WEDP01 core. md – measured data, F – fitting function, P – pedogenic component, LSD – long-term suspension dust component, SSD – short-term suspension dust component, ES – eolian saltation component, LC – lacustrine suspension component, FC – fluvial suspension component, FS – fluvial saltation component.

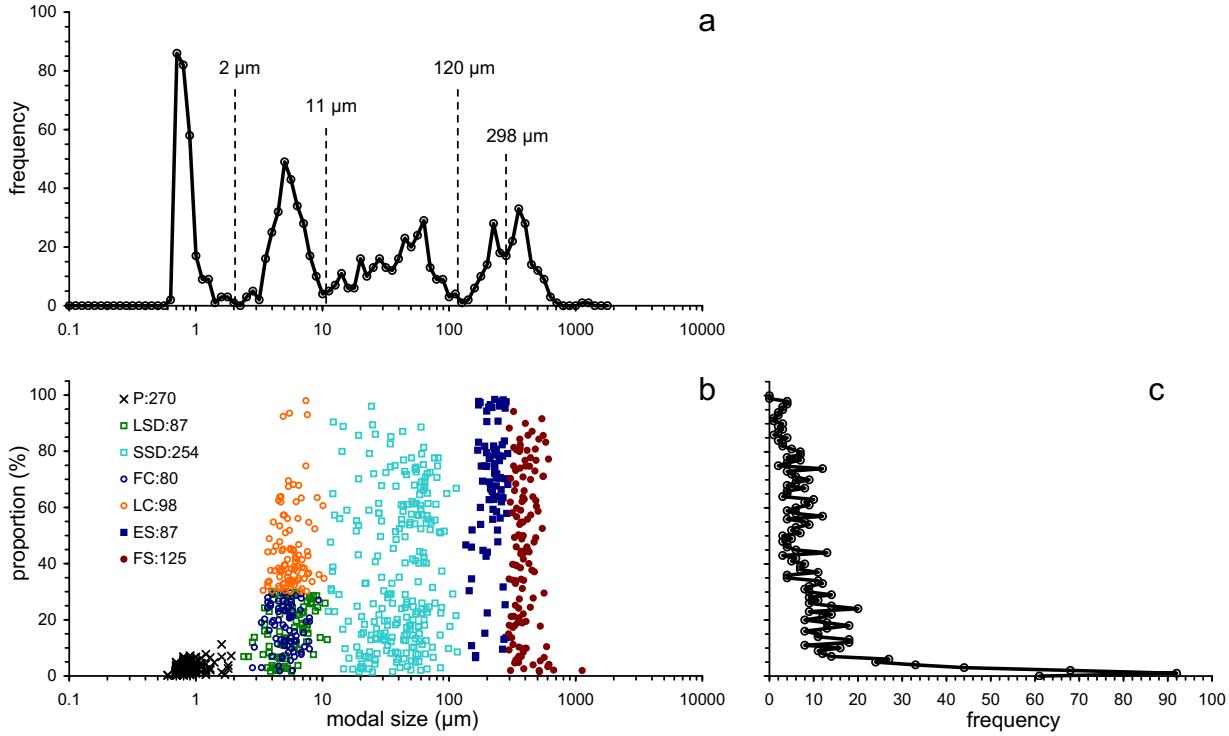

Fig. 3. The statistic plots for sediment components origin analysis. a, The frequency of modal sizes of all components of whole samples; b, proportion-modal size plot; and c, the frequency of proportions. Frequency is the number of components.

group between 11 and 120 μm is corresponding to short-term suspension dust with the modal size between 40 and 60 μm, which is the typical modal size of the coarse component of loess (Sun et al., 2002, 2004, 2008); the group between 120 and 298 μm with the modal size of ~220 μm is correlated with the eolian sand component; and the >298 μm group with the modal size of ~360 μm is corresponding to the fluvial sand component.

The group between 2 and 11 μm with the modal size of ~5 μm is the combination of the long-term suspension eolian dust (fine eolian dust), long-term fluvial suspension component (fluvial clay) and lacustrine suspension component (lacustrine clay), because they own nearly same modal size range. However, they can be almost distinguished from the "frequency-proportion" curve (Fig. 3c). The frequency obviously decreases at ~8%, ~30% and ~80% in proportion. The ~8% and ~80% inflections are corresponding to the reducing of pedogenic components and suspension (long-term and short-term) components, respectively; the ~30% inflection is related to the main decrease of the 2–11 μm group (153 components < 30%, 98 components > 30%). According to the lithological characteristics and the typical components fitting, the few typical lacustrine silty clay deposits in WEDP01 core own a high proportion of lacustrine suspension component. Therefore, the proportion more than 30% components with modal size between 2 and 11 μm represent the lacustrine suspension components, and indicating a main lacustrine sedimentary environment. Below 30%, its type is determined by the original type of main saltation/short-term suspension component, because the minor component is the attachment to the main component in the same sedimentary system. On this basis, one fluvial suspension component is corresponding to a main fluvial sand component, and one long-term suspension dust component is correlated to a main eolian saltation component or a main short-term suspension dust component (see Fig. 3b).

ESR dating was accomplished in the Chronology Laboratory, Institute of Geology, China Earthquake Administration. Rock magnetic, paleomagnetic and grain-size measurements were performed at the Key Laboratory of Western China's Environment systems of the Ministry of Education, Lanzhou University. SEM samples were analyzed in the Key Laboratory for Magnetism and Magnetic Materials of the Ministry of Education, Lanzhou University.

4. Results

4.1. Rock magnetic and paleomagnetic results

The pilot samples are grouped into two types according to the shapes of hysteresis loops and *M–T* curves (magnetization vs. temperature) (Fig. 4). Magnetite is revealed as predominant magnetic carriers of the first type as indicated by the fast decrease of the magnetization at ~580 °C (0–48.3 m, Fig. 4b, d) and typical hysteresis loops of multidomain magnetite (Thompson and Oldfield, 1986, Fig. 4a, c). For the second type, the main drop of magnetization occurs at ~650 °C suggesting hematite as the main magnetic minerals in the strata of 48.3–276 m (Fig. 4f, h, j, l). Moreover, the typical wasp-waisted hysteresis loops (Fig. 4e, g, i, k) suggest the co-existence of both low and high coercivity minerals (Roberts et al., 1995; Tauxe et al., 1996).

The systematic demagnetization diagrams for representative samples from both normal and reversed polarities are shown in Fig. 5. In general, a low temperature component was removed by heating to ~210 °C or occasionally up to 330 °C. After removing this component, the remanent magnetization decays toward the origin representing the characteristic remanent magnetization (ChRM). The ChRM directions were determined by at least four steps with maximum angular deviation (MAD) less than 15°. 451 sample data were removed, most of which were composed of medium to coarse sand and gravels maintaining unstable ChRM. Ten samples with shallow inclination (absolute values less than 5°) were also excluded from the results to avoid misleading in determination of

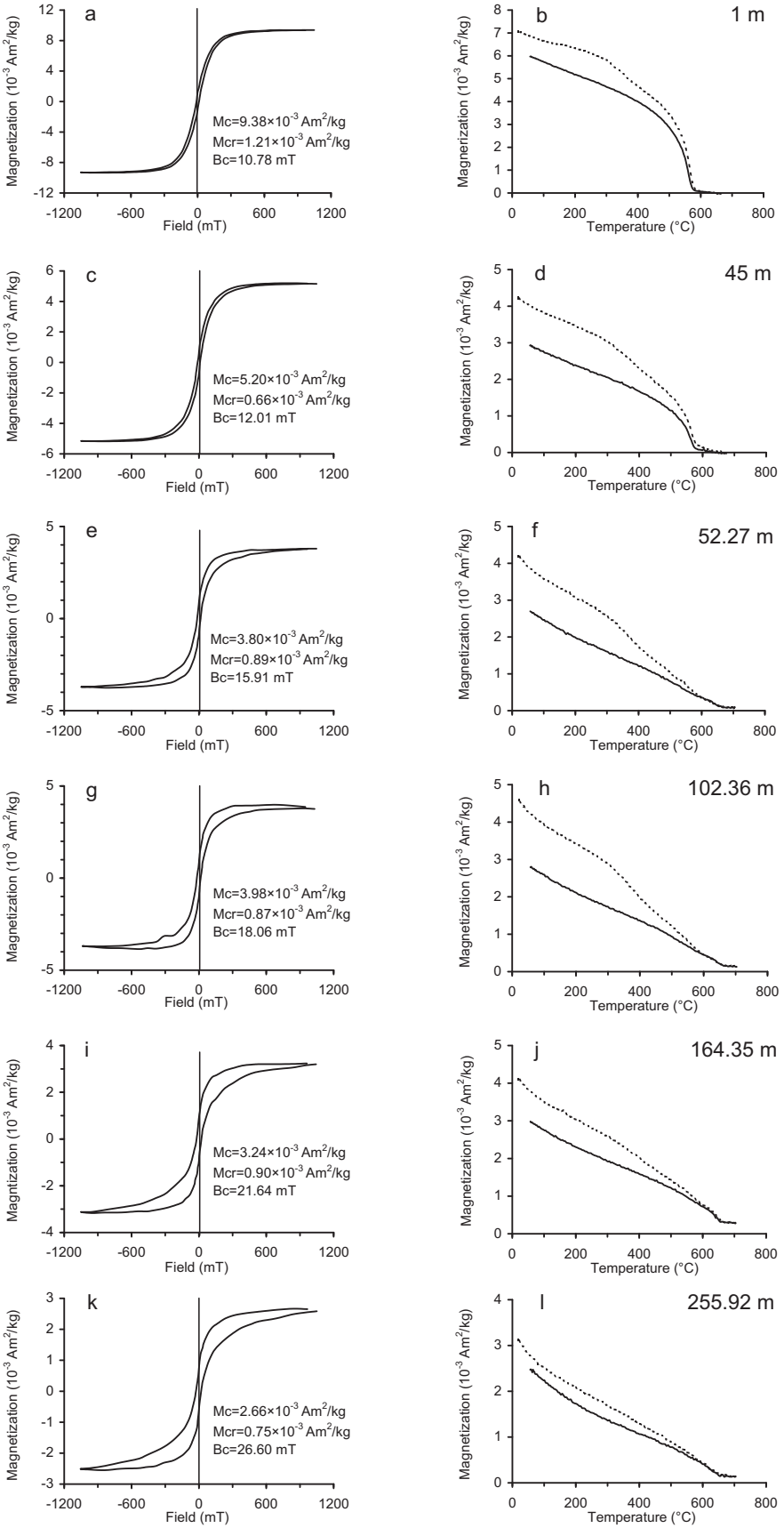

Fig. 4. Magnetic hysteresis loops (left) and thermomagnetic curves (right) for representative samples from the WEDP01 core. The broken (continuous) line represents the heating (cooling) curve.

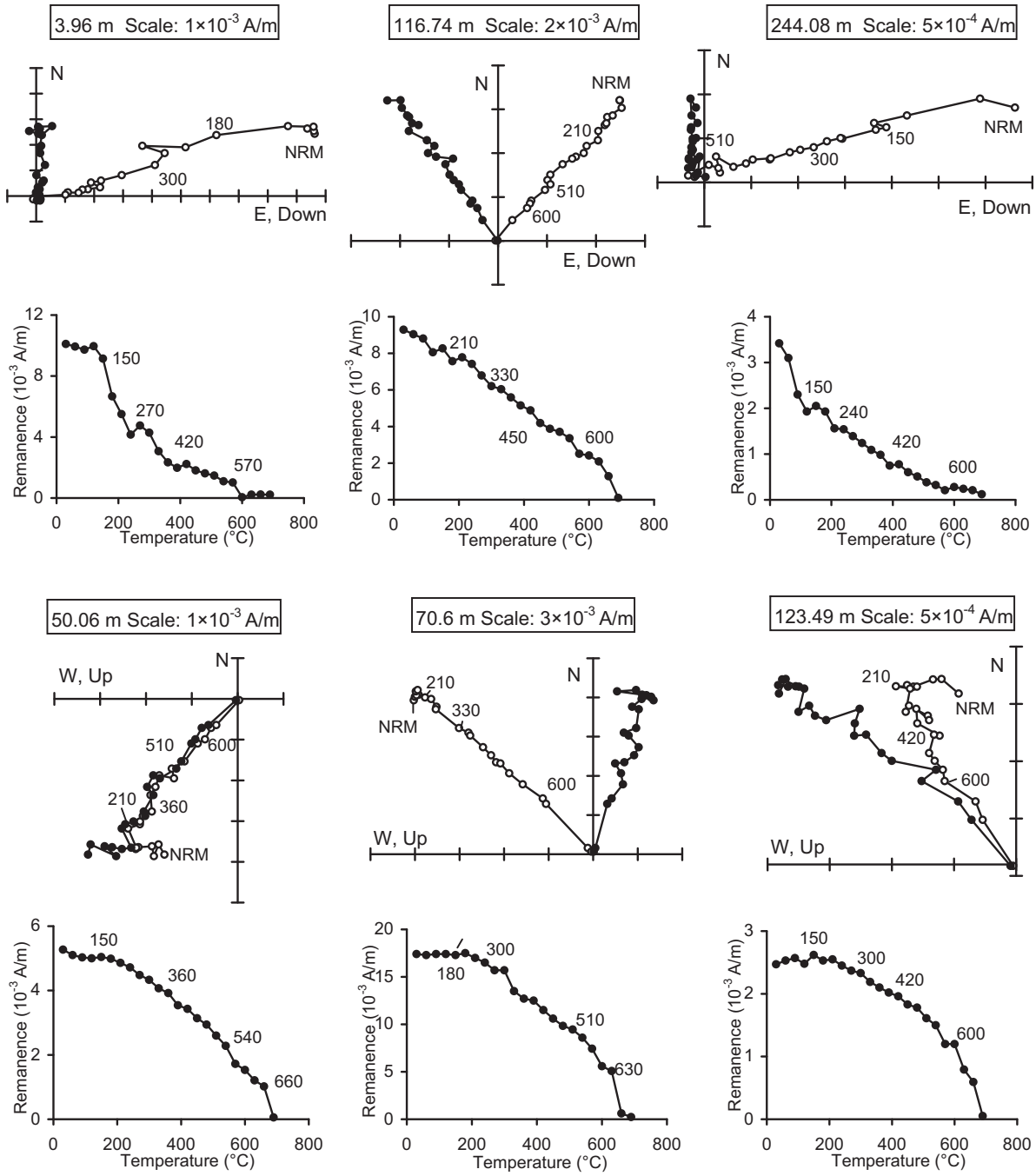

Fig. 5. Orthogonal demagnetization diagrams and remanence intensity plots of the typical normal and reversed samples from the WEDP01 core. The solid (open) circles represent the horizontal (vertical) plane.

the polarity zones. Since no valid declination data is available for these core samples, the magnetic polarity sequence is constructed based on inclination values of the WEDP01 core.

The accepted 735 inclinations are shown in Fig. 6 with 3° intervals. Generally, both positive and negative inclinations follow normal distribution. The mean positive and negative inclinations are calculated by the Arason-Levi method based on maximum likelihood estimation (Arason and Levi, 2010). When applying a reversal test, each polarity zone is considered as a single site and the inclinations which is less than ±15° or more than ±75° are excluded for these directions may represent polarity transition period. Total 649 out of 735 inclinations were in calculating with 88.3% acceptability rate. The site-mean inclinations are listed on Table 1. The mean normal inclination is 49.78° and that of reversed inclination is −45.03°. The inclination difference between the normal and reversed inclinations is less than 5° that suggests they are antipodal. The passage of the reversal test of the datasets suggests that the inclinations of WEDP01 core are reliable to reconstruct the polarity sequence.

The magnetic polarity chrons are defined by at least three successive data points which span more than 1 m. Ten normal and nine reversed polarity zones are observed from the WEDP01 core

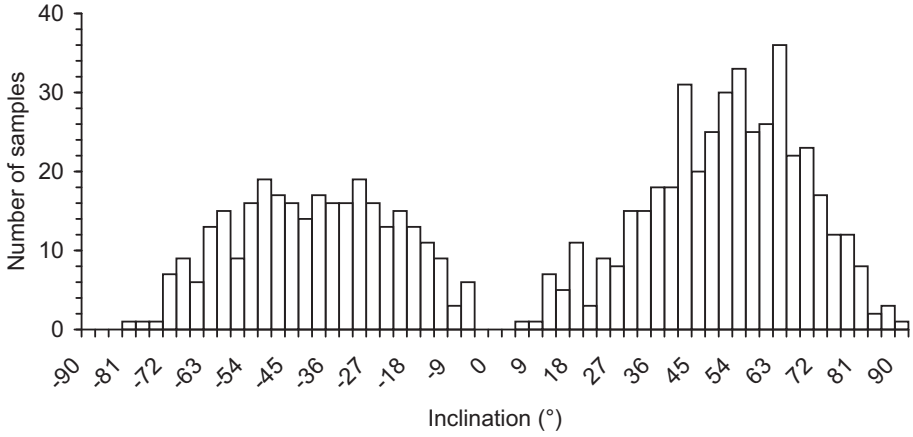

Fig. 6. Histogram of reliable inclinations of the WEDP01 core with 3° windows.

(Fig. 7). The N7 and R9 are not definite with four dispersive inclination values, probably because of the poor recovery and unstable ChRM in sand and gravels layers. The reconstructed polarity sequence can be clearly matched to the standard geomagnetic polarity time scale (GPTS) (Cande and Kent, 1995; Laj and Channell, 2007). The topmost normal polarity zone N1 (0–33.17 m) is correlated to C1n (Brunhes Normal Polarity Chron), and the sequence comprising the reversed zones R1–R7 are interpreted as C1r–C2r (Matuyama Reversed Polarity Chron). The long normal polarity zones N8–N10 with two short reversed polarity zones (R8, R9) are corresponded to C2nAn (Gauss Normal Polarity Chron). Based on these correlations, the short normal polarity zones N3 (59–60.82 m), N4 (76.5–78.35 m), N5 (96.2–100.06 m), N6 (106.42–119.36 m) and N7 (124.3–129.79 m) should correspond to Jaramillo (C1r.1n), Cobb Mt., Gilsa, Olduvai (C2n), and Rèunion (C2r.1n), respectively. The short normal polarity zone N2 (45.81–48.17 m) between C1n and C1r.1n was also recorded in the high-resolution loess magnetostratigraphy in Luochuan (Liu et al., 2010a), and may be correlated with Kamikatsura or Santo Rosa. The two short reversed polarity zones N8 (198.43–203.03 m) and N9 (216.96–225.66 m) correspond to the C2nAn.1r (Keana) and C2nAn.2r (Mammoth), respectively. Based in the above correlations, the boundary of Brunhes/Matuyama (B/M) and Matuyama/Gauss (M/G) boundaries are located at 33.17 and 144.02 m, respectively. Unfortunately, the bottom of C2nAn was not recorded and the bottom age (~3.55 Ma) of the core strata has to be obtained by extrapolation.

The age–depth plot is presented in Fig. 8a. The slope shifts from 128.94 between 2.581 and 3.55 Ma to 51.191 between 0 and 2.581 Ma, revealing the high accumulation rate during late Pliocene. This is consistent with the accumulation rate shown in Fig. 8b, which was calculated from the reversal points revealed from the magnetostratigraphy of WEDP01 core.

The results of ESR dating show that the age of the samples at 10.81, 14.92, 20.50, 25.25 and 30.31 m is 0.548 ± 0.066, 0.638 ± 0.083, 0.506 ± 0.066, 0.705 ± 0.092, and 0.586 ± 0.078 Ma, respectively (Fig. 7). These results are consistent with our paleomagnetic chronology, within the uncertainties inherent in ESR dating.

Table 1
Statistic paleomagnetic results from the WEDP01 core. N – Number of samples, I – Mean inclination, κ – Precision parameter, θ_{63} – Angular standard deviation, α_{95} – 95% confidence limits.

	N	I (°)	κ	θ_{63} (°)	α_{95} (°)
N1	11	62.38	33.64	13.96	7.99
N2	8	52.63	6.9	31.14	22.71
N3	6	37.41	33.37	14.02	11.77
N4	5	50.73	16.45	20.02	19.43
N5	9	27.18	90.57	8.5	5.44
N6	45	52.55	17.06	19.66	5.31
N7	3	39.09	9.12	27.01	43.44
N8	157	46.79	18.07	19.1	2.72
N9	45	57.7	24.73	16.3	4.36
N10	103	58.87	15.79	20.44	3.62
R1	29	−45.26	8.79	27.52	9.58
R2	45	−43.86	13.25	22.34	6.07
R3	29	−51.59	14.8	21.12	7.2
R4	63	−40.37	16.23	20.16	4.58
R5	27	−45.76	20.16	18.07	6.34
R6	24	−34.32	19.04	18.6	6.96
R7	31	−52.96	18.19	19.03	6.23
R8	5	−41.25	7.6	29.63	35.67
R9	4	−47.58	13.5	22.13	25.95
Normal		49.78	29.16	15	9.1
Reversed		−45.03	111.15	7.67	4.9

4.2. Sedimentary facies

Commonly, eolian sands show rounded to sub-rounded shapes with dish-shaped depressions. The loess grains are of irregular shapes and have dish-shaped depressions. In contrast, the lacustrine–fluvial sands show sub-rounded shaped with striations; the alluvial–fluvial chaotic deposits contain angular coarse quartz with fresh fractures and irregular fine grains (Xie, 1984). According to these characteristics, the sample at 19.1 m (Fig. 2a 2) is typical eolian sand like the modern dune (Fig. 2a 1); the sample at 40.04 m (Fig. 2a 3) contains dominant eolian sands with minor fine grains (Fig. 2a 3); the sample at 60.97 m (Fig. 2a 4) is suggested as dust deposits like loess; the sample at 117.91 m (Fig. 2a 5) is fluvial sands mixed with fine grains; and the sample at 223.49 m (Fig. 2a 6) signals alluvial chaotic deposits.

Fig. 9 shows the proportion and modal size variations of each component. From the combination of each component, the WEDP01 core could be divided into five units:

Unit 1: 201.94–276 m, chaotic alluvial–fluvial deposits mixed with little eolian dust. Fluvial sand is main component in this unit (mean proportion is nearly 50%), combining with fluvial clay. Lacustrine clay is separated in some interlayer with relatively lower proportion (less than 60%). The most gravels samples are with low proportion (less than 30%), and the proportion of eolian dust is lower too.

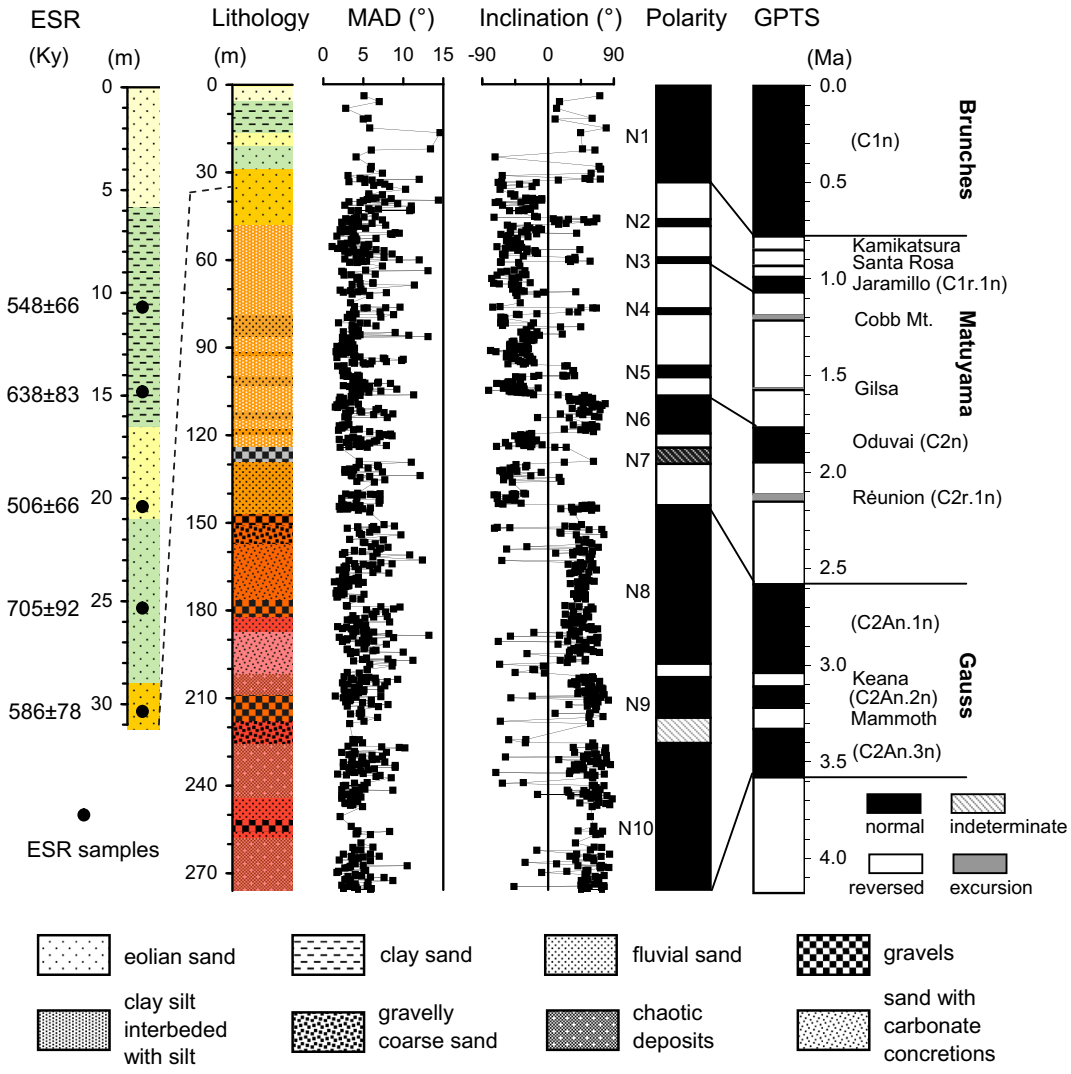

Fig. 7. ESR dating, Lithology and magnetostratigraphy of the WEDP01 core. The main standard geomagnetic polarity time scale (GPTS) is from Cande and Kent (1995); excursions are from Laj and Channell (2007).

Unit 2: 147–201.94 m, fluvial–lacustrine deposits mixed with little eolian dust. The gravels disappear except at the two typical gravels layers. Fluvial sand and clay and lacustrine clay are dominant in the deposits alternately, with little eolian dust as unit 1.

Unit 3: 78.9–147 m, eolian dust mixed with fluvial–lacustrine deposits relative to units 1 and 2 with a high proportion of dust. The proportion of eolian dust fast increases and dominates in some layers alternating with fluvial sand and lacustrine clay. In this unit, just one gravels layer is located between 124.15 and 129.41 m (proportion is ~30%).

Unit 4: 48.3–78.9 m, eolian dust mixed with lacustrine clay. Fluvial components disappear, and just two eolian components and lacustrine clay dominate the deposits alternately.

Unit 5: 0–48.3 m, eolian sand interbedded with lacustrine deposits. Eolian sand is dominated in this unit (mean proportion 73%). Lacustrine clay and fluvial sand are just found in two layers at 11 and 26–29 m in this unit. The pedogenic component also suddenly drops obviously from a high proportion (4.3%) between 48.3 and 78.9 m (2.6% between 48.3 and 276 m) to a relatively lower level between 0 and 48.3 m (1.4%). Although the proportion of eolian dust in this unit is sufficiently low and suddenly drops at 48.3 m (26.6% between 28.99 and 48.3 m), it becomes much lower above 28.99 m (18.3% between 0 and 28.99 m). In contrast, the mean size and the proportion of eolian sand significantly increase (from 166.8 μm to 199.4 μm and 67.3% to 76.6%, respectively). In other words, this unit could be subdivided into two subunits at the boundary depth of 28.99 m.

In summary, based on the visual inspection of core and analysis of grain morphology and grain-size, the sediments of the WEDP01 core can be classified into 5 groups: 1) Alluvial–fluvial deposits mixed with a little eolian dust from ~3.55 to 3.09 Ma (201.94–276 m); 2) Fluvial–lacustrine deposits mixed with eolian dust from 3.09 to 2.6 Ma (147–201.94 m); 3) Eolian dust mixed with the fluvial–lacustrine deposits from 2.6 to 1.22 Ma (78.9–147 m); 4) Eolian dust mixed with lacustrine clay from 1.22 to 0.9 Ma (48.3–78.9 m); and 5) Dominant eolian sand mixed with dust from 0.9 Ma to present (0–48.3 m).

5. Discussion

In the WEDP01 core, the continuous appearance of eolian sand (73% in average) occurred after ~0.9 Ma (Fig. 10), although the

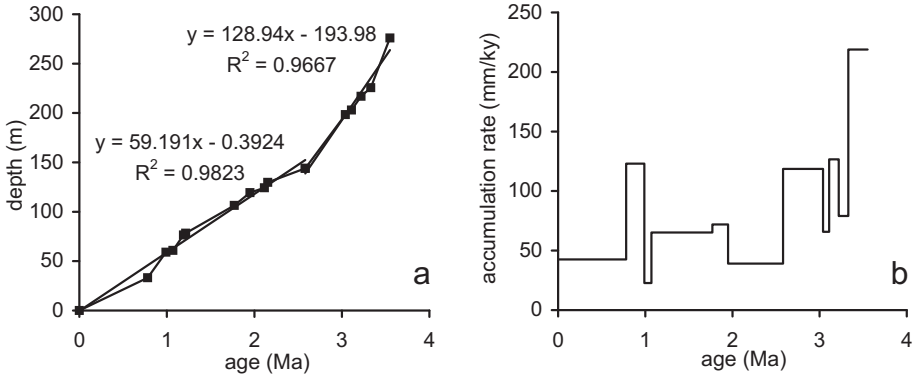

Fig. 8. Depth–age plot (a) for the WEDP01 core based on correlation with the geomagnetic polarity time scale. Accumulation rates plot (b) is calculated from the sediment thickness between correlated chronologic boundaries.

eolian sand component was found in few intervals in the core of 0.9–3.55 Ma (53% in average) which are best interpreted as local wind-blown sand activities such as regional intermittent short-term riparian eolian sand deposits. Thus, formation of the Tengger Desert did not occur until 0.9 Ma. In 0.9–0.68 Ma, the proportion of eolian dust and pedogenic component were still with a relatively high level in comparison to 0.68–0 Ma, revealing a relatively humid desert environment. After 0.68 Ma, the eolian sand component became overwhelmingly dominant in the sediments, suggesting further drying and final formation of the Tengger Desert as present.

The drying during 0.9–0.68 Ma is well documented in the loess records near the southwestern Tengger Desert. The bottom age of ~0.85 Ma Wuwei loess section (Guan et al., 2011) was interpreted as a piece of evidence of Tengger Desert formation. In the distal desert areas, loess records reveal expansion of distal Taklimakan Desert (Fang et al., 2002a) and Gurbantunggut Desert (Fang et al., 2002b) at 0.9–0.8 Ma. Also, the accumulation rate of the Chashmanigar loess-paleosol sequence in southern Tajikistan increased after ~0.8 Ma (Ding et al., 2002), and degree of chemical weathering weakened significantly after 0.85–0.6 Ma (Yang et al., 2006), revealing intensified aridity and expansion of the deserts in Central Asia.

On the CLP, dramatic dryings were documented in many loess records. Increased accumulation rates and grain-size are reported to occur at 0.9–0.8 Ma from the Lanzhou loess sequence in the northwestern CLP (Chen and Zhang, 1993), and the Xifeng, Zhaojiachuan and Luochuan loess sequences in the main CLP (Sun et al., 2008). The >125 μm dust content in the Jingbian loess-paleosol sequence, northern margin of CLP near the Mu Us Desert, increased dramatically after ~0.7 Ma (Ding et al., 2005). The pollen record at the Chaona loess sequence on the CLP reveals a shift from forest-steppe (pine-grass) to open forest-steppe (mesophilous and xeromorphic herbs-pine) at ~0.95 Ma, indicating intensified aridification (Wu et al., 2007). The carbon isotope record of the Lingtai loess sequence reveals the expansion of C_4 plant at 0.9 Ma (An et al., 2005). The chemical weathering weakened after 1.0–0.8 Ma according to the $^{86}Sr/^{87}Sr$ record from the Lingtai loess sequence (Chen et al., 2001; Wang et al., 2007), consistent with the increase $(CaO + Na_2O + MgO)/TiO_2$ ratios after 0.85 Ma (Yang et al., 2006).

This mid-Pleistocene drying event is also preserved in the sedimentary basins in the northwestern China. The evaporate mineral records in the Qahansilatu Playa in the western Qaidam Basin reveal that intensified evaporation started from ~1.0 to 0.9 Ma, which became more apparently after ~0.65 Ma (re-calculated from the accumulation rate of the core) (Li et al., 2010). The pollen records of the borehole SG-3 in the Fengxi Salina Plain in the western Qaidam Basin reveal that desert vegetation (*Chenopodiaceae*, *Ephedraceae*) started to develop at 0.9 Ma, and *Ephedraceae*-dominated vegetation prevails after 0.6 Ma (Cai et al., 2012).

Although proximal deserts in China have been assumed to be the source regions of the CLP (Liu, 1985; Liu et al., 1994; Zhang et al., 1997, 2003; Sun, 2002; Rao et al., 2006; Chen et al., 2007; Lü and Sun, 2011), our study reveals that the dust emission of Tengger Desert is probably not very high compared with times after mid-Pleistocene. The obvious increase of sedimentary accumulation rate on the CLP by ~0.9 Ma (e.g. Chen and Zhang, 1993; Sun et al., 2008) and slight increase by ~0.9–0.8 Ma in the North Pacific Ocean (Rea et al., 1998) are probably the dust responses to the formations and/or expansions of the proximal deserts and the expansion of dust source areas in mid-Pleistocene.

The uplift of the Tibetan Plateau during mid-Pleistocene (e.g. Amano and Taira, 1992; Cui et al., 1998; Li and Fang, 1999; Song et al., 2001, 2005; Wu et al., 2001; Zhao et al., 2001; Chen et al., 2005; Fang et al., 2005; Sakai et al., 2006; Liu et al., 2010b; Zhang et al., 2012) had been proposed as the main drying force, which could result in at least four effects for desert formation over its northern and northeastern areas: 1) The uplift greatly blocks monsoon moisture to reach interior Asian resulting to a very drying local climate for desert formation. Modeling experiments showed that the northern and northeastern arid area near the plateau were relatively humid before the uplift (e.g. Ruddiman and Kutzbach, 1989; Manabe and Broccoli, 1990; Kutzbach et al., 1993); and present climatic work demonstrated these areas were not influenced by the Indian Ocean moisture (Tian et al., 2001, 2007; Wu, 2009). 2) The uplift of Tibetan Plateau significantly strengthened the atmospheric circulations, especially in dust seasons. Climatic analysis and modeling works consistently proved that winter monsoon circulations were obviously strengthened over areas like Tengger Desert (e.g. Kutzbach et al., 1993; An et al., 2001; Liu and Yin, 2002). 3) The previous relatively high tableland in the northern and northeastern plateau became sedimentary basins after the uplifts; the Badain Jaran desert and Tengger Desert in the Alxa Plateau are two typical ones of this kind basins (Zhu et al., 1980; Wu, 2009). 4) The uplift resulted in sufficient classic sediments to be carried in fluvial and alluvial activities flowing from mountains down to these sedimentary basins. These classic sediments are the source materials and finally sorted by wind and transported to desert areas to form eolian sand. The large fluvial fans of Shiyanghe River and Heihe River in the upwind area of the Tengger Desert and Badain Jaran Desert have been proved to demonstrate genetic relation among mountain uplift, fluvial activity and desert formation (Zhu et al., 1980; Wu, 2009; Yang et al., 2012). In addition, the ice volume increase during the Mid-Pleistocene Transition (MPT) (e.g. Ruddiman et al., 1989; Mudelsee and Schulz, 1997; Clark et al., 2006) is another plausible driver for Asian drying (e.g. Ding et al.,

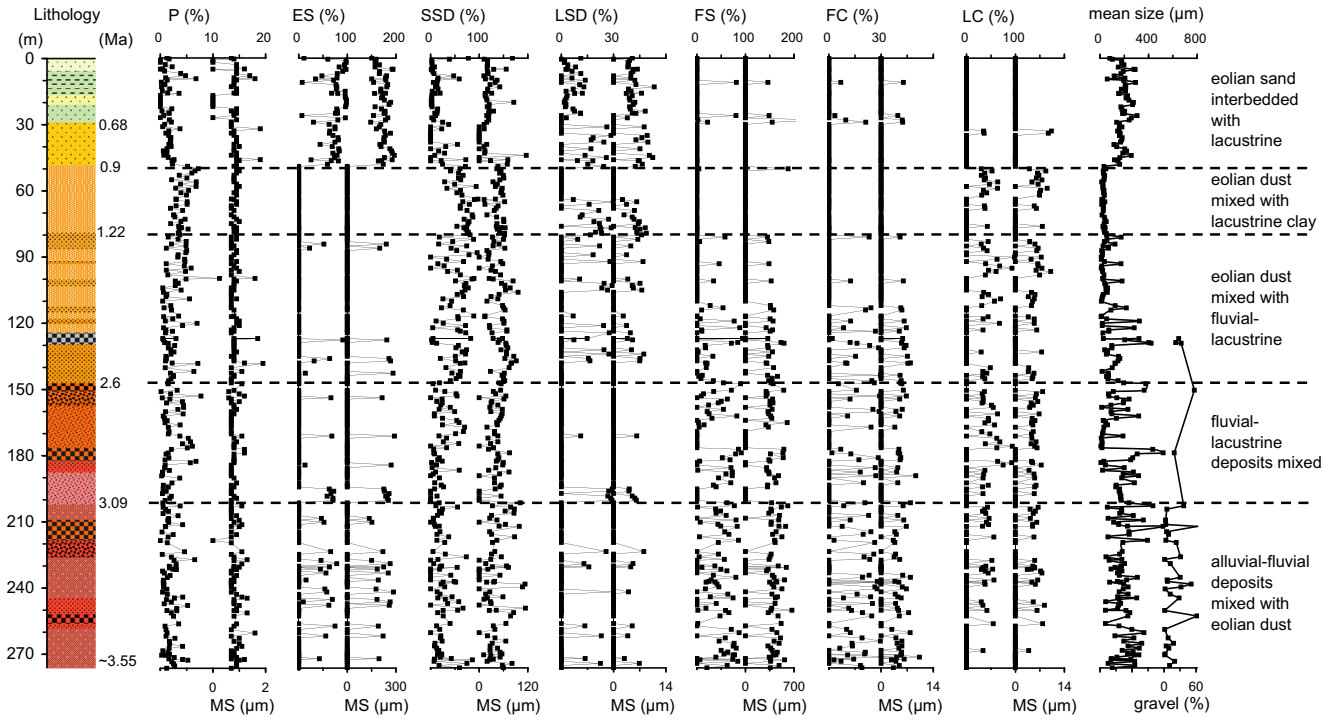

Fig. 9. Variations of mean size, proportion of gravel, proportion and modal size (MS) of various original components of the WEDP01 core. The explanation to modal size is given in text.

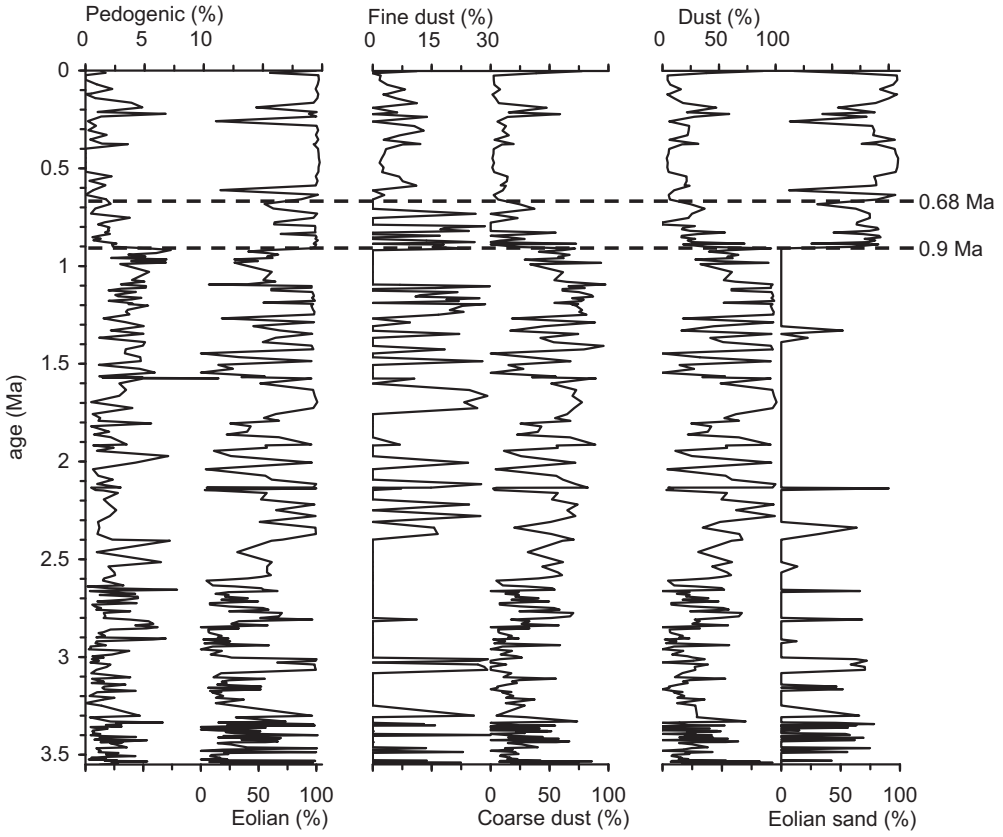

Fig. 10. Time series of arid proxies from the WEDP01 core. Dust proportion is the sum of fine (long-term suspension) and coarse (short-term suspension) and dust components; eolian proportion is the sum of dust and eolian sand.

1995; Shackleton et al., 1995; Liu and Ding, 1998; Lu et al., 2010), although the climatic mechanism is complicated.

6. Conclusion

The 276 m WEDP01 core strata in the central Tegger Desert is composed of alluvial–fluvial deposits, lacustrine–fluvial deposits mixed with dust in the lower part, and eolian sand on the upper part. Paleomagnetic study with ESR dating indicates that the core spans from ~3.55 Ma to the present, and that the B/M and M/G boundaries are determined at the depth of 33.17 m and 144.02 m, respectively. The continuous eolian sand component appeared by ~0.9 Ma, revealing initial formation of the Tengger Desert; and dominate proportion of eolian sands in the strata since ~0.68 Ma indicates the expansion of the Tengger Desert. Formation of the proximal deserts might be a direct cause for increased dust input to the CLP and the North Pacific Ocean after ~0.9 Ma.

Acknowledgments

This study is supported by the National Science Foundation of China grants (41272045, 41130102, 41172329 and 40876025), National Basic Research Program of China (2012CB956102, 2010CB833401), and National Innovative Research Team Project (41021091). We are grateful to Prof. Junsheng Nie for careful English correction, Dr. Zhiyu Yi and Dr. Chengyin Liu for their comments and suggestions on this paper, Jianping Li for the ESR measurement, Lei Gu for his hard work on sampling, and Qian Xue, Guoqiang Li for their hard fieldwork.

Appendix A. Supplementary material

Supplementary data related to this article can be found at http://dx.doi.org/10.1016/j.quascirev.2013.12.003.

References

Amano, K., Taira, A., 1992. Two-phase uplift of Higher Himalayas since 17 Ma. Geology 20, 391–394.
An, Z.S., Kutzbach, J.E., Prell, W.L., Porter, S.C., 2001. Evolution of Asian monsoons and phased uplift of the Himalaya–Tibetan plateau since Late Miocene times. Nature 411, 62–66.
An, Z.S., Huang, Y.S., Liu, W.G., Guo, Z.T., Colman, S., Li, L., Warren, P., Ning, Y.F., Cai, Y.J., Zhou, W.J., Lin, B.H., Zhang, Q.L., Cao, Y.N., Qiang, X.K., Chang, H., Wu, Z.K., 2005. Multiple expansions of C4 plant biomass in East Asia since 7 Ma coupled with strengthened monsoon circulation. Geology 33, 705–708.
An, Z., Colman, S.M., Zhou, W., Li, X., Brown, E.T., Jull, A.J.T., Cai, Y., Huang, Y., Lu, X., Chang, H., Song, Y., Sun, Y., Xu, H., Liu, W., Jin, Z., Liu, X., Cheng, P., Liu, Y., Ai, L., Li, X., Liu, X., Yan, L., Shi, Z., Wang, X., Wu, F., Qiang, X., Dong, J., Lu, F., Xu, X., 2012. Interplay between the Westerlies and Asian monsoon recorded in Lake Qinghai sediments since 32 ka. Sci. Rep. 2, 619. http://dx.doi.org/10.1038/srep00619.
Arason, P., Levi, S., 2010. Maximum likelihood solution for inclination-only data in paleomagnetism. Geophys. J. Int. 182, 753–771.
Ashley, G.M., 1978. Interpretation of polymodal sediments. J. Geol. 86, 411–421.
Bagnold, R.A., Barndorff-Nielsen, O., 1980. The pattern of natural size distributions. Sedimentology 27, 199–207.
Cai, M., Fang, X., Wu, F., Miao, Y., Appel, E., 2012. Pliocene–Pleistocene stepwise drying of Central Asia: evidence from paleomagnetism and sporopollen record of the deep borehole SG-3 in the western Qaidam Basin, NE Tibetan Plateau. Global Planet. Change 94–95, 72–81.
Cande, S.C., Kent, D.V., 1995. Revised calibration of the geomagnetic polarity timescale for the Late Cretaceous and Cenozoic. J. Geophys. Res. 100, 6093–6095.
Cao, J.X., Wang, S.H., Yuan, X.F., Cheng, J.R., 1985. Regional Geological Survey Report and Map (1:200,000) of Chahanbuluge, Inner Mongolia, China. Bureau of Geology and Mineral Resources of Ningxia Hui Autonomous Region, Yin Chuan (in Chinese).
Chen, F.H., Li, J., Zhang, W., 1991. Loess stratigraphy of the Lanzhou profile and its comparison with deep-sea sediment and ice core record. GeoJournal 24, 201–209.
Chen, F.H., Zhang, W.X., 1993. Loess Stratigraphy and Quaternary Glaciation in Gansu–Qinghai Provinces. Science Press, Beijing (in Chinese).
Chen, J., An, Z., Liu, L., Ji, J., Yang, J., Chen, Y., 2001. Variations in chemical compositions of the eolian dust in Chinese Loess Plateau over the past 2.5 Ma and chemical weathering in the Asian inland. Sci. China Ser. D: Earth Sci. 44, 403–413.
Chen, S., Jin, Z., Wang, S., Shen, J., 2005. Late Cenozoic chemical weathering and environmental changes recorded in the Co Ngoin Sediments, Central Qinghai–Tibet Plateau. Acta Geol. Sin. Engl. Ed. 79, 384–391.
Chen, J., Li, G., Yang, J., Rao, W., Lu, H., Balsam, W., Sun, Y., Ji, J., 2007. Nd and Sr isotopic characteristics of Chinese deserts: implications for the provenances of Asian dust. Geochim. Cosmochim. Acta 71, 3904–3914.
Clark, P.U., Archer, D., Pollard, D., Blum, J.D., Rial, J.A., Brovkin, V., Mix, A.C., Pisias, N.G., Roy, M., 2006. The middle Pleistocene transition: characteristics, mechanisms, and implications for long-term changes in atmospheric pCO_2. Quatern. Sci. Rev. 25, 3150–3184.
Cui, Z., Wu, Y., Liu, G., Ge, D., Pang, Q., Xu, Q., 1998. On Kunlun–Yellow River tectonic movement. Sci. China Ser. D: Earth Sci. 41, 592–600.
Ding, Z., Liu, T., Rutter, N.W., Yu, Z., Guo, Z., Zhu, R., 1995. Ice-volume forcing of east Asian winter monsoon variations in the past 800 000 years. Quatern. Res. 44, 149–159.
Ding, Z.L., Sun, J.M., Yang, S.L., Liu, T.S., 1998. Preliminary magnetostratigraphy of a thick eolian red clay-loess sequence at Lingtai, the Chinese Loess Plateau. Geophys. Res. Lett. 25, 1225–1228.
Ding, Z.L., Rutter, N.W., Sun, J.M., Yang, S.L., Liu, T.S., 2000. Re-arrangement of atmospheric circulation at about 2.6 Ma over northern China: evidence from grain size records of loess-palaeosol and red clay sequences. Quatern. Sci. Rev. 19, 547–558.
Ding, Z.L., Ranov, V., Yang, S.L., Finaev, A., Han, J.M., Wang, G.A., 2002. The loess record in southern Tajikistan and correlation with Chinese loess. Earth Planet. Sci. Lett. 200, 387–400.
Ding, Z.L., Derbyshire, E., Yang, S.L., Sun, J.M., Liu, T.S., 2005. Stepwise expansion of desert environment across northern China in the past 3.5 Ma and implications for monsoon evolution. Earth Planet. Sci. Lett. 237, 45–55.
Fang, X.M., Lü, L.Q., Yang, S.L., Li, J.J., An, Z.S., Jiang, P.A., Chen, X.L., 2002a. Loess in Kunlun Mountains and its implications on desert development and Tibetan Plateau uplift in west China. Sci. China Ser. D: Earth Sci. 45, 290–299.
Fang, X.M., Shi, Z.T., Yang, S.L., Yan, M.D., Li, J.J., Jiang, P.A., 2002b. Loess in the Tian Shan and its implications for the development of the Gurbantunggut Desert and drying of northern Xinjiang. Chin. Sci. Bull. 47, 1381–1387.
Fang, X., Zhao, Z., Li, J., Yan, M., Pan, B., Song, C., Dai, S., 2005. Magnetostratigraphy of the late Cenozoic Laojunmiao anticline in the northern Qilian Mountains and its implications for the northern Tibetan Plateau uplift. Sci. China Ser. D: Earth Sci. 48, 1040–1051.
Guan, Q.Y., Pan, B.T., Li, N., Zhang, J.D., Xue, L.J., 2011. Timing and significance of the initiation of present day deserts in the northeastern Hexi Corridor, China. Palaeogeogr. Palaeoclimatol. Palaeoecol. 306, 70–74.
Guo, Z.T., Ruddiman, W.F., Hao, Q.Z., Wu, H.B., Qiao, Y.S., Zhu, R.X., Peng, S.Z., Wei, J.J., Yuan, B.Y., Liu, T.S., 2002. Onset of Asian desertification by 22 Myr ago inferred from loess deposits in China. Nature 416, 159–163.
Guo, Z.T., Peng, S.Z., Hao, Q.Z., Biscaye, P.E., An, Z.S., Liu, T.S., 2004. Late Miocene–Pliocene development of Asian aridification as recorded in the Red-Earth Formation in northern China. Global Planet. Change 41, 135–145.
Hakanson, L., Jansson, M., 1983. Principles of Lake Sedimentology. Springer-Verlag, Berlin.
Kirschvink, J.L., 1980. The least-squares line and plane and the analysis of palaeomagnetic data. Geophys. J. Roy. Astronom. Soc. 62, 699–718.
Kukla, G., An, Z., 1989. Loess stratigraphy in Central China. Palaeogeogr. Palaeoclimatol. Palaeoecol. 72, 203–225.
Kutzbach, J.E., Prell, W.L., Ruddiman, W.F., 1993. Sensitivity of Eurasian climate to surface uplift of the Tibetan Plateau. J. Geol., 177–190.
Laj, C., Channell, J.E.T., 2007. Geomagnetic excursions. In: Kono, M. (Ed.), Treatise on Geophysics, Geomagnetism, vol. 5. Elsevier, Amsterdam, pp. 373–416.
Li, J., Fang, X., 1999. Uplift of the Tibetan Plateau and environmental changes. Chin. Sci. Bull. 44, 2117–2124.
Li, M., Fang, X., Yi, C., Gao, S., Zhang, W., Galy, A., 2010. Evaporate minerals and geochemistry of the upper 400 m sediments in a core from the Western Qaidam Basin, Tibet. Quatern. Int. 218, 176–189.
Liu, C., Masuda, A., Okada, A., Yabuki, S., Fan, Z., 1994. Isotope geochemistry of Quaternary deposits from the arid lands in northern China. Earth Planet. Sci. Lett. 127, 25–38.
Liu, T.S., 1985. Loess and the Environment. China Ocean Press, Beijing.
Liu, T., Ding, Z., 1998. Chinese loess and the paleomonsoon. Annu. Rev. Earth Planet. Sci. 26, 111–145.
Liu, X., Yin, Z., 2002. Sensitivity of East Asian monsoon climate to the uplift of the Tibetan Plateau. Palaeogeogr. Palaeoclimatol. Palaeoecol. 183, 223–245.
Liu, W.M., Zhang, L.Y., Sun, J.M., 2010a. High resolution magnetostratigraphy of Luochuan loess-paleosol sequence in the central Chinese Loess Plateau. Chin. J. Geophys. 53, 888–894 (in Chinese with English abstract).
Liu, D., Fang, X., Song, C., Dai, S., Zhang, T., Zhang, W., Miao, Y., Liu, Y., Wang, J., 2010b. Stratigraphic and paleomagnetic evidence of mid-Pleistocene rapid deformation and uplift of the NE Tibetan Plateau. Tectonophysics 486, 108–119.
Lu, H., Wang, X., Li, L., 2010. Aeolian sediment evidence that global cooling has driven late Cenozoic stepwise aridification in central Asia. In: Geological Society, London, Special Publications, vol. 342, pp. 29–44.
Lü, T., Sun, J., 2011. Luminescence sensitivities of quartz grains from eolian deposits in northern China and their implications for provenance. Quatern. Res. 76, 181–189.

Manabe, S., Broccoli, A.J., 1990. Mountains and arid climates of middle latitudes. Science 247, 192–195.
Mudelsee, M., Schulz, M., 1997. The Mid-Pleistocene climate transition: onset of 100 ka cycle lags ice volume build-up by 280 ka. Earth Planet. Sci. Lett. 151, 117–123.
Qiang, M.R., Chen, F.H., Zhang, J.W., Zu, R.P., Jin, M., Zhou, A.F., Xiao, S., 2007. Grain size in sediments from Lake Sugan: a possible linkage to dust storm events at the northern margin of the Qinghai–Tibetan Plateau. Environ. Geol. 51, 1229–1238.
Qiang, X.K., Li, Z.X., Powell, C.M., Zheng, H.B., 2001. Magnetostratigraphic record of the Late Miocene onset of the East Asian monsoon, and Pliocene uplift of northern Tibet. Earth Planet. Sci. Lett. 187, 83–93.
Qiang, X.K., An, Z.S., Song, Y.G., Chang, H., Sun, Y.B., Liu, W.G., Ao, H., Dong, J.B., Fu, C.F., Wu, F., Lu, F.Y., Ca, Y.J., Zhou, W.J., Cao, J.J., Xu, X.W., Ai, L., 2011. New eolian red clay sequence on the western Chinese Loess Plateau linked to onset of Asian desertification about 25 Ma ago. Sci. China Ser. D: Earth Sci. 54, 136–144.
Rao, W., Yang, J., Chen, J., Li, G., 2006. Sr–Nd isotope geochemistry of eolian dust of the arid-semiarid areas in China: implications for loess provenance and monsoon evolution. Chin. Sci. Bull. 51, 1401–1412.
Rea, D.K., Snoeckx, H., Joseph, L.H., 1998. Late Cenozoic eolian deposition in the North Pacific: Asian drying, Tibetan uplift, and cooling of the northern hemisphere. Paleoceanography 13, 215–224.
Roberts, A.P., Cui, Y.I., Verosub, K.L., 1995. Wasp-waisted hysteresis loops: mineral magnetic characteristics and discrimination of components in mixed magnetic systems. J. Geophys. Res. 100, 17909–17924.
Ruddiman, W.F., Kutzbach, J.E., 1989. Forcing of late Cenozoic northern hemisphere climate by plateau uplift in southern Asia and the American west. J. Geophys. Res. Atmos. 94, 18409–18427.
Ruddiman, W.F., Raymo, M.E., Martinson, D.G., Clement, B.M., Backman, J., 1989. Pleistocene evolution: northern hemisphere ice sheets and North Atlantic Ocean. Paleoceanography 4, 353–412.
Sakai, H., Sakai, H., Yahagi, W., Fujii, R., Hayashi, T., Upreti, B.N., 2006. Pleistocene rapid uplift of the Himalayan frontal ranges recorded in the Kathmandu and Siwalik basins. Palaeogeogr. Palaeoclimatol. Palaeoecol. 241, 16–27.
Shackleton, N., An, Z., Dodonov, A., Gavin, J., Kukla, G., Ranov, V., Zhou, L., 1995. Accumulation rate of loess in Tadjikistan and China: relationship with global ice volume cycles. Quatern. Proc. 4, 1–6.
Song, C., Fang, X., Li, J., Gao, J., Zhao, Z., Fan, M., 2001. Tectonic uplift and sedimentary evolution of the Jiuxi Basin in the northern margin of the Tibetan Plateau since 13 Ma BP. Sci. China Ser. D: Earth Sci. 44, 192–202.
Song, C., Gao, D., Fang, X., Cui, Z., Li, J., Yang, S., Jin, H., Douglas, B.,L.,K.J., 2005. Late Cenozoic high-resolution magnetostratigraphy in the Kunlun Pass Basin and its implications for the uplift of the northern Tibetan Plateau. Chin. Sci. Bull. 50, 1912–1922.
Song, Y., Fang, X., Torii, M., Ishikawa, N., Li, J., An, Z., 2007. Late Neogene rock magnetic record of climatic variation from Chinese eolian sediments related to uplift of the Tibetan Plateau. J. Asian Earth Sci. 30, 324–332.
Sun, D.H., Shaw, J., An, Z.S., Chen, M.Y., Yue, L.P., 1998a. Magnetostratigraphy and paleoclimatic interpretation of continuous 7.2 Ma Late Cenozoic eolian sediments from the Chinese Loess Plateau. Geophys. Res. Lett. 25, 85–88.
Sun, D.H., An, Z.S., Shaw, J., Bloemendal, S.J., Sun, Y.B., 1998b. Magnetostratigraphy and palaeoclimatic significance of Late Tertiary eolian sequences in the Chinese Loess Plateau. Geophys. J. Int. 134, 207–212.
Sun, D.H., Bloemendal, J., Rea, D.K., Vandenberghe, J., Jiang, F.C., An, Z.S., Su, R.X., 2002. Grain-size distribution function of polymodal sediments in hydraulic and eolian environments, and numerical partitioning of the sedimentary components. Sediment. Geol. 152, 263–277.
Sun, D., Bloemendal, J., Rea, D.K., An, Z., Vandenberghe, J., Lu, H., Su, R., Liu, T., 2004. Bimodal grain-size distribution of Chinese loess, and its palaeoclimatic implications. Catena 55, 325–340.
Sun, D.H., Su, R.X., Bloemendal, J., Lu, H.Y., 2008. Grain-size and accumulation rate records from Late Cenozoic aeolian sequences in northern China: implications for variations in the East Asian winter monsoon and westerly atmospheric circulation. Palaeogeogr. Palaeoclimatol. Palaeoecol. 264, 39–53.
Sun, D., Bloemendal, J., Yi, Z., Zhu, Y., Wang, X., Zhang, Y., Li, Z., Wang, F., Han, F., 2011a. Palaeomagnetic and palaeoenvironmental study of two parallel sections of late Cenozoic strata in the central Taklimakan Desert: implications for the desertification of the Tarim Basin. Palaeogeogr. Palaeoclimatol. Palaeoecol. 300, 1–10.
Sun, D., Zhang, Y., Han, F., Zhang, Y., Yi, Z., Li, Z., Wang, F., Wu, S., Li, B., 2011b. Magnetostratigraphy and palaeoenvironmental records for a Late Cenozoic sedimentary sequence from Lanzhou, Northeastern margin of the Tibetan Plateau. Global Planet. Change 76, 106–116.
Sun, D., Su, R., Li, Z., Lu, H., 2011c. The ultrafine component in Chinese loess and its variation over the past 7.6 Ma: implications for the history of pedogenesis. Sedimentology 58, 916–935.
Sun, J.M., 2002. Provenance of loess material and formation of loess deposits on the Chinese Loess Plateau. Earth Planet. Sci. Lett. 203, 845–859.
Sun, J.M., Zhang, Z., Zhang, L., 2009. New evidence on the age of the Taklimakan Desert. Geology 37, 159–162.
Tauxe, L., Mullender, T.A.T., Pick, T., 1996. Potbellies, wasp-waists, and superparamagnetism in magnetic hysteresis. J. Geophys. Res. 101, 571–584.
Thompson, R., Oldfield, F., 1986. Environmental Magnetism. Allen and Unwin, London.
Tian, L., Masson-Delmotte, V., Stievenard, M., Yao, T., Jouzel, J., 2001. Tibetan Plateau summer monsoon northward extent revealed by measurements of water stable isotopes. J. Geophys. Res. 106, 28081–28088.
Tian, L., Yao, T., MacClune, K., White, J.W.C., Schilla, A., Vaughn, B., Vachon, R., Ichiyanagi, K., 2007. Stable isotopic variations in west China: a consideration of moisture sources. J. Geophys. Res. 112, 1–12.
Wang, B.Y., Wang, P.Y., 1997. Notes on the age of the Chaganbulage formation in Haosibuldu Basin, Nei Mongol, China. Vertebrat. Palasiatic. 35, 121–129 (in Chinese with English abstract).
Wang, X., Sun, D., Wang, F., Li, B., Wu, S., Guo, F., Li, Z., Zhang, Y., Chen, F., 2013. A high-resolution multi-proxy record of late Cenozoic environment change from central Taklimakan Desert, China. Clim. Past 9, 2731–2739.
Wang, Y.X., Yang, J.D., Chen, J., Zhang, K.J., Rao, W.B., 2007. The Sr and Nd isotopic variations of the Chinese Loess Plateau during the past 7 Ma: implications for the East Asian winter monsoon and source areas of loess. Palaeogeogr. Palaeoclimatol. Palaeoecol. 249, 351–361.
Wu, F., Fang, X., Ma, Y., Herrmann, M., Mosbrugger, V., An, Z., Miao, Y., 2007. Plio-Quaternary stepwise drying of Asia: evidence from a 3-Ma pollen record from the Chinese Loess Plateau. Earth Planet. Sci. Lett. 257, 160–169.
Wu, Y., Cui, Z., Liu, G., Ge, D., Yin, J., Xu, Q., Pang, Q., 2001. Quaternary geomorphological evolution of the Kunlun Pass area and uplift of the Qinghai–Xizang (Tibet) Plateau. Geomorphology 36, 203–216.
Wu, Z., 2009. Sandy Deserts and its Control in China. Science Press, Beijing (in Chinese).
Xie, Y.Y., 1984. Atlas of Quartz Sand Surface Textural Features of China Micrographs. China Ocean Press, Beijing (in Chinese).
Yang, S., Ding, F., Ding, Z., 2006. Pleistocene chemical weathering history of Asian arid and semi-arid regions recorded in loess deposits of China and Tajikistan. Geochim. Cosmochim. Acta 70, 1695–1709.
Yang, X., Li, H., Conacher, A., 2012. Large-scale controls on the development of sand seas in northern China. Quatern. Int. 250, 74–83.
Yin, G.M., Lin, M., Lu, Y.C., Li, J.P., Han, F., 2007. Preliminary ESR dating results on loess samples from the loess-paleosol sequence at Luochuan, Central Loess Plateau, China. Quatern. Geochronol. 2, 381–385.
Zan, J., Fang, X., Yang, S., Nie, J., Li, X., 2010. A rock magnetic study of loess from the West Kunlun Mountains. J. Geophys. Res. Solid Earth 115, B10101. http://dx.doi.org/10.1029/2009JB007184.
Zhang, X.Y., Arimoto, R., An, Z.S., 1997. Dust emission from Chinese desert sources linked to variations in atmospheric circulation. J. Geophys. Res. 102 (D23), 28041–28047.
Zhang, X.Y., Gong, S.L., Zhao, T.L., Arimoto, R., Wang, Y.Q., Zhou, Z.J., 2003. Sources of Asian dust and role of climate change versus desertification in Asian dust emission. Geophys. Res. Lett. 30, 2272. http://dx.doi.org/10.1029/2003GL018206.
Zhang, W., Appel, E., Fang, X., Song, C., Cirpka, O., 2012. Magnetostratigraphy of deep drilling core SG-1 in the western Qaidam Basin (NE Tibetan Plateau) and its tectonic implications. Quatern. Res. 78, 139–148.
Zhang, K.C., Qu, J.J., Zu, R.P., Han, Q.J., 2008. Dynamical characteristics of wind-blown sand activities at the southeast edge of Tengger Desert: a case study at Shapotou Region. Arid Land Geogr. 31, 643–649 (in Chinese with English abstract).
Zhao, Z., Fang, X., Li, J., Pan, B., Yan, M., Shi, Z., 2001. Paleomagnetic dating of the Jiuquan Gravel in the Hexi Corridor: implication on mid-Pleistocene uplift of the Qinghai–Tibetan Plateau. Chin. Sci. Bull. 46, 2001–2005.
Zhu, Z.D., Wu, Z., Liu, S., Di, X.M., 1980. An Outline of Chinese Deserts. Science Press, Beijing (in Chinese).
Zijderveld, J.D.A., 1967. AC demagnetization of rocks: analysis of results. In: Collison, D.W., Runcorn, S.K., Creer, K.M. (Eds.), Methods in Paleomagnetism. Elsevier, Amsterdam, pp. 254–286.